

Single chain properties of polyelectrolytes in poor solvent

Hans Jörg Limbach, Christian Holm

Max-Planck-Institut für Polymerforschung, Ackermannweg 10, 55128 Mainz, Germany

May 29, 2018

Abstract

Using molecular dynamics simulations we study the behavior of a dilute solution of strongly charged polyelectrolytes in poor solvents, where we take counterions explicitly into account. We focus on the chain conformational properties under conditions where chain-chain interactions can be neglected, but the counterion concentration remains finite. We investigate the conformations with regard to the parameters chain length, Coulomb interaction strength, and solvent quality, and explore in which regime the competition between short range hydrophobic interactions and long range Coulomb interactions leads to pearl-necklace like structures. We observe that large number and size fluctuations in the pearls and strings lead to only small direct signatures in experimental observables like the single chain form factor. Furthermore we do not observe the predicted first order collapse of the necklace into a globular structure when counterion condensation sets in. We will also show that the pearl-necklace regime is rather small for strongly charged polyelectrolytes at finite densities. Even small changes in the charge fraction of the chain can have a large impact on the conformation due to the delicate interplay between counterion distribution and chain conformation.

1 Introduction

Polyelectrolytes (PEs) are polymers which have the ability to dissociate charges in polar solvents resulting in charged polymer chains (macroions) and small mobile counterions [1]. Because of their great relevance in technical applications as well as in molecular biology they enjoy an increasing attention in the scientific community [2, 3, 4, 5]. The combination of macromolecular properties and long-range electrostatic interactions results in an impressive variety of phenomena which makes these systems interesting from a fundamental point of view.

In this paper we focus on the special case of polyelectrolytes under poor solvent conditions. The reason for this is that a large number of polymers are based on a hydrocarbon backbone for which water is a very poor solvent. The solubility in water is often only given due to their charged side groups. Important examples are sulfonated poly-styrene (PSS), poly-

methacrylic acid (PMA), DNA and virtually all proteins. The poor solvent conditions give rise to a competition between the attractive interactions due to the poor solubility of the backbone and the electrostatic repulsion of the PE charges. This can lead to elongated strings of locally collapsed structures (pearls), commonly called pearl-necklaces. Such necklace conformations have been proposed on the basis of fluorescence studies [6]. They have also been predicted in terms of scaling arguments in refs. [7, 8, 9] for a weakly charged single chain PE. Later this has been extended to strongly charged chains and finite concentrations [10, 11, 12, 13]. Also other theoretical approaches support the existence of necklace conformations [14, 15, 16]. The scaling approach of ref. [9] was supplemented with a Monte Carlo simulation of a single chain that shows a cascade from one to two to three globules with increasing strength of the electrostatic repulsion. In their study the polyelectrolyte was weakly charged and every monomer carried a fractional charge. The chain was studied in the infinite dilution limit, where counterions have not to be taken into account. The formation of the necklace structure is due to the Rayleigh instability of a charged droplet which leads to a split once a critical charge is reached. The size of the pearls is determined by the balance between electrostatic repulsion and surface tension. The distance between two pearls is governed by the balance of the electrostatic pearl-pearl repulsion and the surface tension.

Some aspects of the theoretical pearl-necklace picture have been confirmed by simulations using the Debye-Hückel approximation [17, 18] and with explicit counterions [19, 20, 21, 22, 23, 24]. However, there is up to now no clear experimental proof for the existence of necklace chains. Conformational chain properties have been observed which seem to be consistent with the necklace picture [6, 25, 26, 27, 28, 29, 30].

Also the scaling of the peak position of the structure factor q^* with the polymer density ρ has been thoroughly investigated which however reveals only properties that occur in the semi-dilute regime of interacting chains. For good solvent chains in the semi dilute regime the exponent β in the scaling relation $q^* \propto \rho^\beta$ was measured to be $\beta = 0.5$ which is also the theoretically predicted value [31] whereas for poor solvent polyelectrolytes no single value for the exponent seems

to exist. The experimental values vary between $\beta = 0.3$ and $\beta = 0.5$ [32, 33, 34, 35] and show a dependence on the charge fraction of monomers which is implicitly also responsible for the poor solvent parameter of the chain. The theoretical predictions show (for fixed poor solvent and fixed charge fraction) also a complicated transition from a $\beta = \frac{1}{2}$ regime via a $\beta = \frac{1}{3}$ into a crossover scaling [12, 13], whereas recent simulations measured a constant exponent $\beta = \frac{1}{3}$ for the whole concentration range from semi-dilute up into the dense regime [24], so its fair to say that things are far from being well understood.

However, even for the dilute concentration regime, the situation can be more complicated as envisioned in the scaling approach, since the entropy of the chain and of the counterions as well as the electrostatic interaction between counterions and the PE charges have to be taken into account. In our previous shorter communications we reported large conformational fluctuations [22, 23, 24] in the pearl-necklace structures and showed that they were responsible for the absence of strong signatures in the force extension relation and in the form factor.

The aim of the present simulational study is a more detailed investigation of the structure of strongly charged polyelectrolytes in poor solvent in the dilute concentration regime where the chain-chain interaction is weak so that one deals effectively with single chain properties. Our focus will be a thorough data analysis of the observed pearl-necklace conformations. To this end we had to develop a new cluster recognition algorithm that is capable to characterize these interesting conformations automatically from our simulated configurational data. Moreover we look at the stability of the pearl-necklace conformations in the presence of condensed counterions, and perform a study of the Coulomb induced collapse transition. We will compare our results with predictions from scaling theory and will discuss the validity range of the scaling approach for strongly charged chains at finite density. We then attempt to give a preliminary phase diagram for the systems studied. The last part will be devoted to some experimentally accessible observables, like characteristic chain size ratios and form factor. This should be helpful in supporting the evaluation of experimental data in terms of pearl-necklace signatures.

Our paper is organized as follows: After explaining the used simulation method in sec. 2 and giving a short overview over the simulated systems in sec. 3 we will discuss our data analysis methods in sec. 4. In sec. 5 we will compare our results in the pearl-necklace regime with predictions made by scaling theories. In the next sec. 6 we will quantify the role of fluctuations, and describe in sec. 7 our view of the Coulomb induced collapse transition and a preliminary phase diagram for the range of our simulation parameters. We then discuss in detail some measurable observables in sec. 8 and finally end with our conclusion in sec. 9. In the appendix we give a detailed overview of the simulated systems, including a

list of parameters and results for selected basic observables.

2 Simulation method

Our model of a PE solution and our molecular dynamics approach has been described previously in detail in [19, 36, 22]. It consists of N_P flexible bead-spring chains with N_m monomers and N_c counterions which are located in a cubic simulation box of length L with periodic boundary conditions. A fraction f of the monomers is monovalently charged ($\nu_m = 1$). Thus the total charge per chain is $Q_P = fN_m$. The number of counterions which are also monovalently charged ($\nu_c = -1$) is chosen such that the overall system is electrically neutral. Densities are given either as monomer density $\rho_m = N_P N_m / L^3$ or charge density $\rho_c = 2 f N_P N_m / L^3$.

All particles interact via a Lennard-Jones (LJ) potential $4\epsilon[(\frac{\sigma}{r})^{12} - (\frac{\sigma}{r})^6 - c]$ for distances $r < R_c$ and zero elsewhere. The constant c is chosen such that the potential value is zero at the cutoff R_c , and ϵ is a measure of the solvent quality. Monomers interact up to $R_c = 2.5\sigma$ giving them a short range attraction which can be tuned by changing the value of ϵ . The counterions interact via a purely repulsive LJ interaction with $R_c = 2^{1/6}\sigma$. The units of length, energy and time are σ , ϵ , and τ , respectively.

The chain monomers are in addition connected along the chain by the finite extendible nonlinear elastic (FENE) bond potential of the form $-14k_B T \ln[1 - (r/(2\sigma))^2]$ which results in an average bond length $b \approx 1.1\sigma$.

Charged particles with charges q_i and q_j at separation r_{ij} interact via the Coulomb energy $k_B T \ell_B q_i q_j / r_{ij}$ where the Bjerrum length is defined as $\ell_B = e^2 / (4\pi\epsilon_S\epsilon_0 k_B T)$ (e : unit charge, ϵ_0 and ϵ_S : permittivity of the vacuum and of the solvent). The Coulomb interaction was calculated with the P3M-algorithm [37, 38], tuned to force accuracies which are much higher than the thermal noise level.

A velocity Verlet algorithm with a standard Langevin thermostat is used to integrate the equation of motion [39] (friction coefficient $\Gamma = \tau^{-1}$, time step $\Delta t = 0.0125\tau$). Thus the solvent is only implicitly present via its permittivity ϵ_S , the friction constant Γ and the solvent quality parameter ϵ in the LJ potential.

The simulation time after equilibration for all systems was at least 100 times the measured correlation time for the end-to-end distance R_E and the chains centers of mass diffused at least several radii of gyration R_G . The osmotic pressure p was measured to be always positive and additional simulations over a large density range [24] showed that the pV diagram is convex at all densities, thus our simulations are stable, reach true thermal equilibrium, and reside in a one phase region. The volume density inside the pearls does not exceed 0.47 which is below the glass transition. We therefore are certain that

also the pearl formation and restructuring was observed in equilibrium.

3 Simulated systems

We have simulated our poor solvent polyelectrolytes mainly as a function of the parameters chain length N_m , solvent quality ϵ , strength of the electrostatic interaction ℓ_B and the charge fraction f . All simulations are performed in dilute solution such that the interaction between the chains is small. For the system with the longest chains ($N_m = 478$) we have a chain extension $R_E \approx 60\sigma$ and a chain-chain separation $r_{cc} \approx 252\sigma$ which was calculated for a random packing of spheres according to

$$r_{cc} \approx 1.28 \left(\frac{3\pi}{4} \frac{L^3}{N_P} \right)^{1/3}. \quad (1)$$

The screened renormalized monopole interaction U_{cc}^{DH} between two chains can be estimated for this case to be of the order $k_B T$. For our estimate we have used a crude approximation on the Debye-Hückel level. The effective chain charge $Q_{P,\text{eff}} \approx 64$ is calculated by using the counterions within a shell of 3σ around the polyelectrolyte to renormalize the bare charge $Q_P = 160$. The density of the free counterions $\tilde{\rho}_c$ leads a screening constant $\kappa = \sqrt{4\pi\ell_B\tilde{\rho}_c} \approx 0.009\sigma^{-1}$ and as the interaction potential we take $U_{cc}^{\text{DH}} = \ell_B Q_{P,\text{eff}}^2 e^{-\kappa r_{cc}} r_{cc}^{-1} \approx 2.3k_B T$. For this estimate one has to keep in mind that both the used practical definition of the effective charge as well as the screening concept can not be founded on physical principles.

Details about the used parameters and measurements of some basic observables for all simulated systems can be found in appendix A. We have grouped the simulations into series depending on the investigated parameters.

The chain length dependence is studied in simulation series which differ in the line charge density f . For series A1 we use a charge fraction $f = \frac{1}{3}$, and the chain length is varied over one decade in steps of 48 from $N_m = 48$ to 478. Series A2 and A3 are performed at $N_m = 100, 200$ and 300 with $f = \frac{1}{2}$ at slightly different densities.

To study the dependence on the solvent quality we have varied the short range attraction by changing the LJ parameter ϵ between $0.0k_B T$ and $2.0k_B T$ for medium sized chains of length $N_m = 238$ (series B). The Θ -point for this model was determined to be at $\epsilon(\Theta) = 0.34k_B T$ [19]. For most of the other simulations (series A1, A2, A3, C1, C2 and C3) we used $\epsilon = 1.75k_B T$ which is thus deep in the poor solvent regime. This value is chosen for practical reason. In this regime we have found relatively large and stable pearl-necklace conformations which are more easy to investigate.

The effect of the Coulomb interaction is studied via changing the Bjerrum length ℓ_B and the charge fraction f . We simulated chains with length $N_m = 199$ in three

series C1, C2 and C3 with charge fractions $f = 1$, $f = \frac{1}{2}$ and $f = \frac{1}{3}$ respectively. They are performed at the same charge density $\rho_c = 5 \times 10^{-5}\sigma^{-3}$ but they contain different numbers of counterions $N_c = fN_mN_P$ corresponding to the number of charges on the PEs. All three series start out at $\ell_B = 0\sigma$. In Series C1 ℓ_B ranges up to 10σ , in series C2 and C3 up to 9σ . In addition there is a simulation set with shorter chains $N_m = 94$ with $f = \frac{1}{3}$ and a different solvent parameter $\epsilon = 1.5k_B T$ which we only use for the phase diagram (series C4).

The last series contains four simulations with the same value for the scaling variable $\ell_B b^{-1} f^2 = 0.25$ but different $f = 1, \frac{1}{2}, \frac{1}{3}$ and $\frac{1}{4}$ (series D).

4 Observables and data analysis

In this section we define our measured observables and explain in detail how we analyzed our simulated PE conformations. Especially we present the cluster recognition algorithm which we used to automatically classify different pearl-necklace structures.

We denote the position of monomer i with \mathbf{r}_i and the distance between two particles i and j with r_{ij} . The center of mass for the chain is then $\mathbf{R}_s = \frac{1}{N_m} \sum_{i=1}^{N_m} \mathbf{r}_i$ and the center of mass coordinates are $\mathbf{x}_i = \mathbf{r}_i - \mathbf{R}_s$. For the chain extension we use the end-to-end distance

$$R_E^2 = (\mathbf{r}_1 - \mathbf{r}_{N_m})^2, \quad (2)$$

the radius of gyration

$$R_G^2 = \frac{1}{N_m} \sum_{i=1}^{N_m} |\mathbf{x}_i|^2 \quad (3)$$

and the inverse hydrodynamic radius

$$R_H^{-1} = \frac{1}{N_m(N_m - 1)} \sum_{i \neq j}^{N_m} \frac{1}{r_{ij}}. \quad (4)$$

Note that this definition corresponds to the short time diffusion behavior of polymers. For more information on this topic see ref. [40].

For a first structure classification we use two characteristic ratios between the different chain extension observables. The first characteristic ratio is defined as $r = (R_E/R_G)^2$. The second characteristic ratio is $\alpha = R_G/R_H$ which has the advantage of being experimentally accessible [41].

We will also compute the spherically averaged form factor, sometimes also called single chain structure factor, $S_1(q)$ which can be measured in scattering experiments:

$$S_1(q) = \frac{1}{N_m} \sum_{i=1}^{N_m} \sum_{j=1}^{N_m} \frac{\sin(qr_{ij})}{qr_{ij}}. \quad (5)$$

To describe the counterion distribution around polyelectrolytes we use an integrated counterion distribution $P(r)$. The distance d_i of a counterion i from a chain is

defined as the distance of the counterion from its closest monomer in space. We denote the set of counterions belonging to one chain with \mathcal{C} . From this we can calculate $P(r)$ as

$$P(r) = \frac{1}{Q_P} \int_{r'=0}^r dr' \sum_{i \in \mathcal{C}} \delta(r' - d_i) \quad (6)$$

$P(r)$ denotes the fraction of counterions which are inside a shell with radius r around a polyelectrolyte chain. This definition can be used for a large variety of chain conformations.

For an automated analysis of all types of pearl-necklace structures appearing in our configurational data we need a tool to determine for each monomer, to which pearl or string it belongs, and what is the total number of such substructures. First we should state that there is no sharp definition of a pearl or a string. So what we need is a practical approach to the problem. Our guideline in the development of an automated tool for the identification of pearls and strings is that the result should be close to the result which would be obtained by looking at the conformation by eye.

Before we give a detailed explanation of the used cluster recognition algorithm we want to present some other methods that are based on observables which could be accessible with experimental methods. In this way one can also judge how easily these structures can be observed by current experimental techniques.

The local monomer concentration $\rho_m(\mathbf{r})$ of a chain is given by $\rho_m(\mathbf{r}) = \sum_i^{N_m} \delta(\mathbf{r} - \mathbf{r}_i)$. To distinguish the different substructures, pearls and strings, it is better to use a coarse grained local monomer concentration $\rho_m^c(\mathbf{r})$ which is defined as

$$\rho_m^c(\mathbf{r}) = \frac{1}{V_c} \int_{\mathbf{r}' \in V_c} d\mathbf{r}' \rho_m(\mathbf{r}'), \quad (7)$$

where V_c is a spherical volume with radius r_c around \mathbf{r} . This observable is larger in a pearl than in a string. One can calculate $\rho_m^c(\mathbf{r})$ along the backbone as a function of the monomer positions \mathbf{r}_j . This is done for a chain with length $N_m = 382$ from series A1 whose snapshot is shown in fig. 1a. The resulting coarse grained local monomer concentration with $r_c = 4\sigma$ is shown for comparison directly underneath in fig. 1b.

A second approach uses local distances between the monomers which could be probed by NMR experiments [30]. The local distance between monomer j and the monomer $j + n$ which is n monomers apart on the backbone is defined as

$$r_n(j) = \sqrt{(\mathbf{r}_j - \mathbf{r}_{j+n})^2}. \quad (8)$$

From scaling arguments one expects that the local distances inside the compact pearls scale with $r_n \simeq n^{1/2}$ for small n whereas in the extended strings it scales with

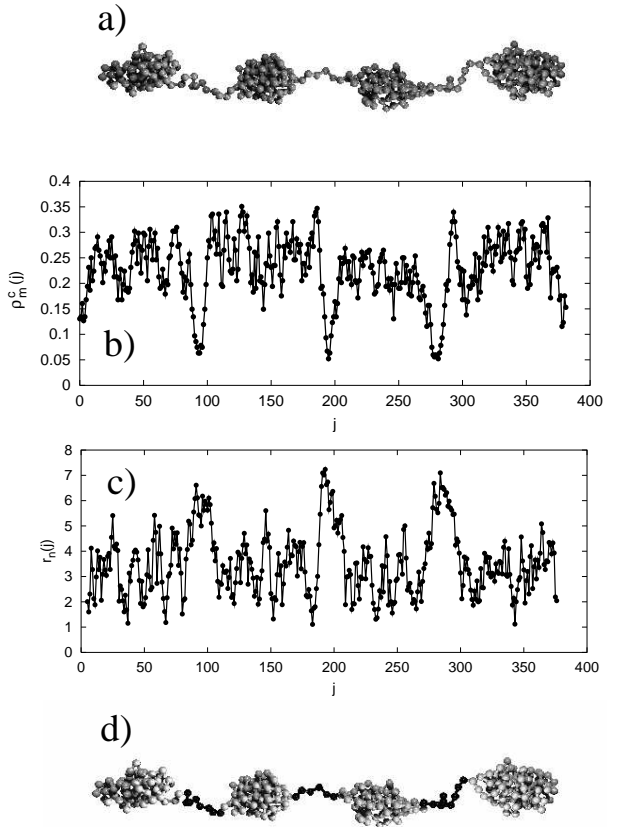


Figure 1. a) Snapshot of a polyelectrolyte chain with $N_m = 382$ from series A1. b) Coarse grained local monomer concentration $\rho_m^c(j)$ with $r_c = 4\sigma$ along the backbone. c) Local distances $r_n(j)$ for $n = 10$ along the backbone. d) Analysis with the cluster recognition algorithm. Monomers in pearls are grey and monomers in strings black.

$r_n \simeq n$. The symbol \simeq is used to state a scaling relation which ignores numerical prefactors. For the conformation shown in fig. 1a the local distances along the backbone are shown for $n = 10$ in fig. 1c.

In both cases one can see the position of the 4 pearls and 3 strings. The problem is that the variation of both $\rho_m^c(\mathbf{r})$ and $r_n(j)$ is of the same order as the difference between the mean values in pearls and strings.

Since the two previous methods have several problems with the structure recognition of pearl-necklace conformations we have developed a more reliable algorithm based on a simple cluster recognition. The question whether a group of monomers forms a cluster is often connected to a distance criterion, e.g. monomers with a distance smaller than a critical value belong to the same cluster. For a polymer one has also to take into account the chain connectivity. This implies that a pure distance criterion is not sufficient. Therefore we require in addi-

tion that there are a certain number of bonds between a pair of monomers along the chain contour. The resulting algorithm is iterative and contains the following steps:

1. At the beginning every monomer is a cluster of size 1 (size = number of monomers belonging to a cluster).
2. Two clusters \mathcal{C}_1 and \mathcal{C}_2 are merged if they contain a pair of monomers ij with $i \in \mathcal{C}_1$, $j \in \mathcal{C}_2$ and $r_{ij} < r_c$. In addition i and j are further apart than n_c bonds along the chain contour: $|i - j| > n_c$.
3. Step 2 is repeated between all clusters as long as one finds clusters that have to be merged.
4. Remove loops: a cluster \mathcal{C}_1 where all monomers are inside (along the chain contour) of another cluster \mathcal{C}_2 are merged. Note that this step is only suitable for polyelectrolytes, but e.g. is not applicable for polyampholytes.
5. Practical definition of pearls: all clusters with a size larger than or equal p_c are pearls. Pearls which are connected directly along the chain contour are merged.
6. Practical definition of strings: all clusters with a size smaller than p_c belong to strings. Strings which are connected directly along the chain contour are merged.
7. Remove dangling ends and merge them to the end pearls. We do this because we have so far not seen dangling ends containing more than 3 monomers which could be seen as an extra string.

Thus the algorithm has in principle three free parameters: r_c , n_c and p_c . But looking at the involved structures, one can establish relations between these parameters which can be used as a rough guide in choosing them. From scaling arguments we know that the distance of two monomers i and j with a distance $|i - j|$ along the chain contour scales as $|i - j|^{1/2}$ inside the pearls and with $|i - j|$ inside the strings. Thus we can choose $bn_c^{1/2} < r_c < bn_c$ to distinguish the two cases. For a weakly charged chain one can determine a suitable value for p_c with help of the pearl size defined in eq. 13. But this is not possible for our strongly charged systems with their subtle dependence on the counterion distribution. The whole data analysis in this paper is done with an empirical parameter set: $r_c = 2.1\sigma$, $n_c = 6$ and $p_c = 9$. Beside extended visual checks we have tested that small changes of the three parameters do not have a significant effect on the final result. The derived sizes for the substructures contain a systematic error of ± 4 monomers coming from the two outer monomers on each side of a substructure, for which one can not decide whether they belong to the next pearl or the next string. A typical result for a structure type with 4 pearls is shown in fig. 1 d. The four

pearls and three strings contain the following numbers of monomers: 90 - 8 - 94 - 6 - 77 - 9 - 98. We do not claim that this is the fastest or the best way to identify pearl-necklace structures, but it worked well when compared with visual checks and thus served our purpose. For an average pearl size larger than 30 monomers it yields a reliability well above 95%.

5 Scaling

One of our goals in this paper is to show to what extend scaling theories that are made for long chains at infinite dilution can be expected to work for dilute PE systems with finite length at finite density. The scaling theory predicts the dependencies of observables like the chain extension on various parameters, e.g. N_m , ℓ_B , f and the reduced temperature τ_r . Here we give only a short overview of some results of the scaling theory for the pearl-necklace regime of polyelectrolytes. For the pearl-necklace regime one finds the following relations [9, 10, 17]: End-to-end distance R_E

$$R_E \simeq N_m b^{1/2} \ell_B^{1/2} f \tau_r^{-1/2}, \quad (9)$$

number of pearls n_P

$$n_P \simeq N_m b^{-1} \ell_B f^2 \tau_r^{-1}, \quad (10)$$

string length l_S

$$l_S \simeq b^{3/2} \ell_B^{-1/2} f^{-1} \tau_r^{1/2}, \quad (11)$$

pearl size (radius) r_P

$$r_P \simeq b^{4/3} \ell_B^{-1/3} f^{-2/3}, \quad (12)$$

pearl size (number of monomers) g_P

$$g_P \simeq b \ell_B^{-1} f^{-2} \tau_r, \quad (13)$$

density inside the pearls ρ_P :

$$\rho_P \simeq b^{-3} \tau_r. \quad (14)$$

Note that r_P is independent of the solvent quality, and that our solvent quality parameter ϵ is proportional to the second virial coefficient of the LJ potential and hence also proportional to the reduced temperature τ_r .

5.1 Scaling variable chain length N_m

The linear scaling of R_E with N_m is caused by the electrostatic repulsion of the chain charge and is dominated by the string length l_S . Due to the finite length of our systems we have to correct the scaling relation given in eq. 9. For small chain length, $N_m \leq g_P$, the chain conformation consists of one pearl. The size of this pearl scales as $N_m^{1/3}$. Thus we have to replace N_m by $(N_m - g_P)$ in eq. 9. In fig. 2 a linear relation between R_E and $(N_m - g_P)$

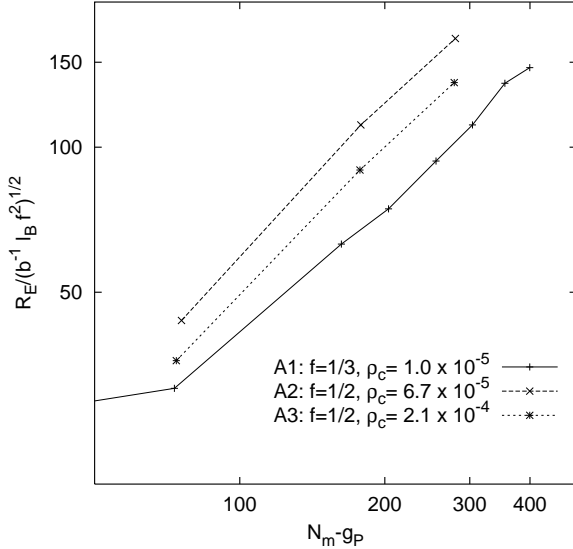


Figure 2. Scaling plot for R_E versus $(N_m - g_P)$ (see eq. 9). The series A1, A2 and A3 differ in the charge fraction f and the density ρ_c . One can see that R_E scales linearly with $(N_m - g_P)$, but the prefactor is not constant.

can be observed. But the full scaling relation from eq. 9 including the parameters specifying the Coulomb interaction, namely f , is not valid. Series A1 is performed at $f = \frac{1}{3}$ and its density is in between that of series A2 and A3 which have both $f = \frac{1}{2}$.

We find a similar result for the number of pearls n_P in the pearl-necklace regime. The scaling relation for n_P versus $(N_m - g_P)$ (see eq. 10) is shown for the data from series A1, A2 and A3 in fig. 3. Again there is a linear relation between n_P and N_m but different prefactors for different values of f and ρ_c .

To get some visual impression, we show in fig. 4 some snapshots of simulations with different chain length N_m from series A1. The discreteness of the pearl number n_P does not play a significant role for sufficiently long chains which give rise at least to a dumbbell. Then our data is in accord with the scaling relations for the quantities pearl size, string length and pearl density, namely they are constant within the statistical error. We find for the systems of series A1 with $N_m > 200$: $g_P = 78 \pm 4$, $\rho_P = 0.67 \pm 0.04\sigma^{-3}$ and $l_S = 7.3 \pm 2\sigma$. As we will show later, the discreteness of the number of pearls is smeared out due to fluctuations between different structure types in a way that the average quantities can maintain their optimal values, compare also section 6.

5.2 Solvent quality ϵ

In the simulation series B we have tested the behavior of polyelectrolyte chains upon changing the solvent quality via the Lennard-Jones parameter ϵ . Since the practically

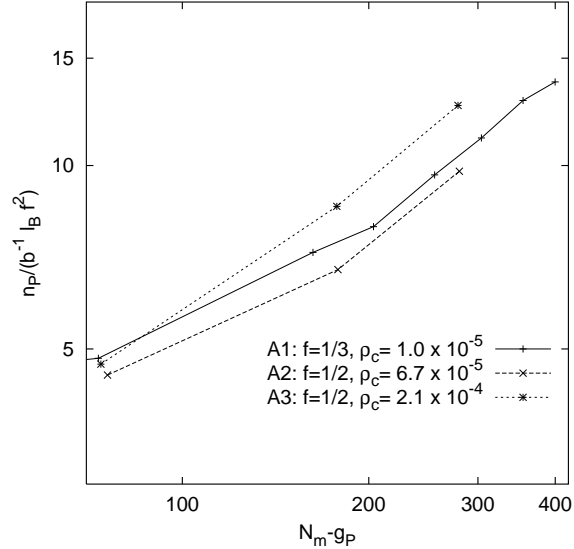


Figure 3. Scaling plot for n_P versus $(N_m - g_P)$ (see eq. 10) for series A1, A2 and A3.

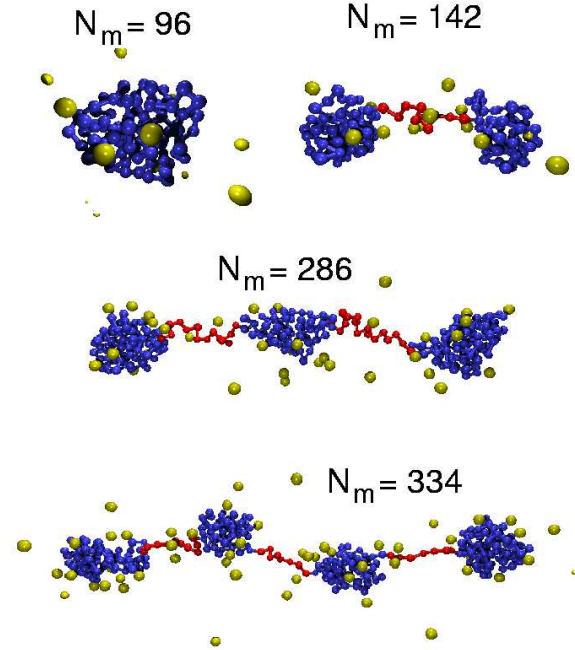


Figure 4. Snapshots from series A1 with different chain length N_m and different number of pearls n_P .

usable range for this parameter is small, ranging from $\epsilon = 0k_B T$ to $2.0k_B T$, it is not possible to test the scaling predictions over a large parameter range. In addition the range of ϵ values for which we observed pearl-necklace structures is even smaller, namely from $\epsilon = 1.0k_B T$ to $2.0k_B T$. For values of $\epsilon < 1.0k_B T$ one leaves the poor

solvent regime and for values $\epsilon > 2k_B T$ we encounter simulational problems, e.g. kinetically frozen states. The dependence of R_E and n_P on ϵ is shown in fig. 5 and fig. 6. For both observables the scaling predictions seem

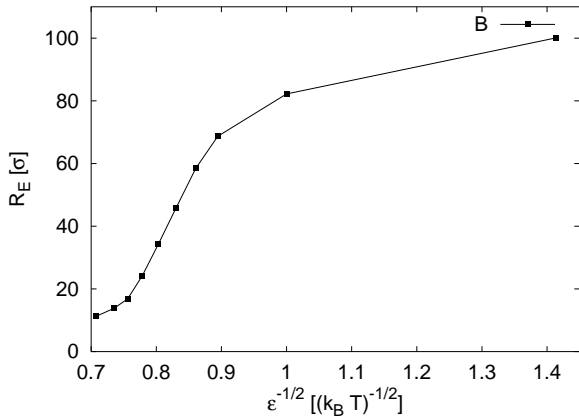


Figure 5. Dependence of R_E on the solvent quality parameter ϵ (simulation series B).

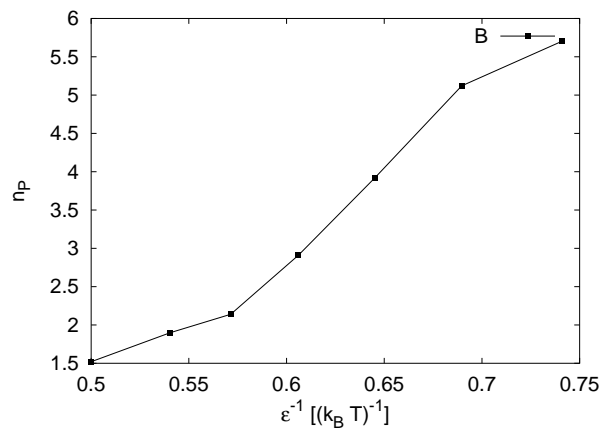


Figure 6. Dependence of n_P on the solvent quality parameter ϵ (simulation series B).

to hold for a small ϵ -region. R_E scales linear with $\epsilon^{-1/2}$ in the range from $\epsilon = 1.25k_B T$ to $\epsilon = 1.75k_B T$ (see eq. 9). The regime where n_P scales as ϵ^{-1} is even smaller and extends from $\epsilon = 1.45k_B T$ to $\epsilon = 1.75k_B T$ (see eq. 10). In the same regime also the density inside the pearls ρ_P which is plotted against ϵ in fig. 7 shows a linear dependence on ϵ as predicted by eq. 14. However, a more reliable conclusion may be drawn from the scaling relation for the pearl size r_P , since r_P should be independent of the solvent quality (see eq. 12). We therefore have calculated the pearl size as $r_P = \frac{3}{4}\pi g_P \rho_P^{-1/3}$ from our simulation data and plotted it versus ϵ . As can be seen in fig. 8 r_P increases monotonically with ϵ , hence shows an unexpected dependency on ϵ . We are lead therefore to

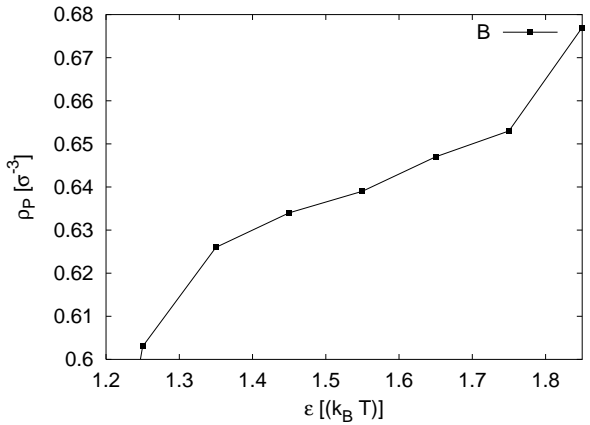


Figure 7. Dependence of ρ_P on the solvent quality parameter ϵ (simulation series B).

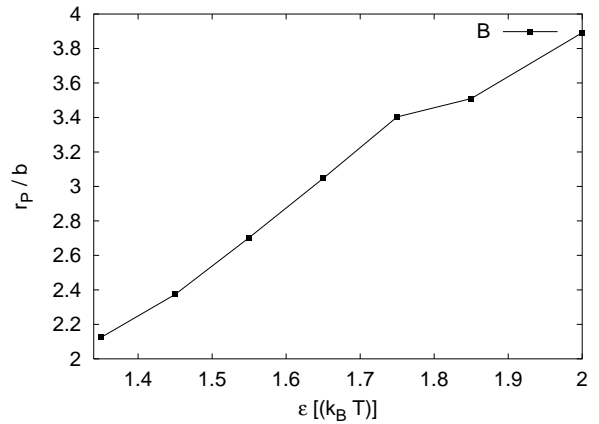


Figure 8. Dependence of r_P on the solvent quality parameter ϵ (simulation series B).

conclude that the scaling predictions for the dependency on the solvent quality do not work here. They fail for the most definite test case, the independence of the pearl radius r_P of the solvent quality. Nevertheless in a small regime for $\epsilon/(k_B T) = 1.45 \dots 1.75$ they seem to work approximately for some observables due to a fortuitous error cancellation.

To elucidate the role of the finite counterion density around the chains we calculated the integrated ion distribution $P(r)$ (see eq. 6). In fig. 9 $P(r)$ is shown for different solvent qualities. The counterion distribution changes greatly close to the chain with ϵ . In the pearl-necklace regime between $\epsilon/(k_B T) = 1.0$ and $\epsilon/(k_B T) = 1.85$ which is the same regime where we find also the strongest change in the chain extension we observe that the counterion distribution is changing the most. The fraction of counterions being very close to the chain which hence can be called condensed is also varying strongly. Only the top four curves show an inflection

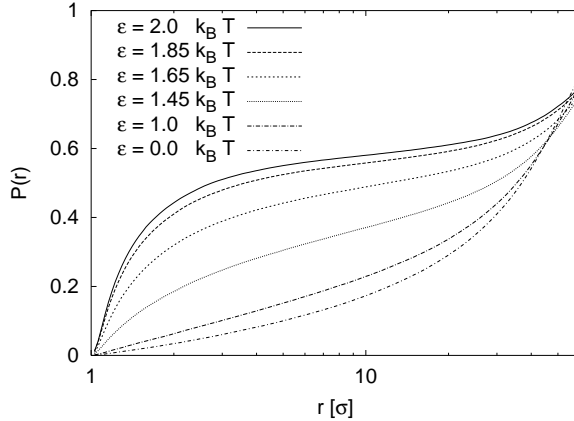


Figure 9. Integrated counterion distribution $P(r)$ around polyelectrolyte chains subject to different solvent qualities.

point which is a sign of counterion condensation [42, 43] (see also sec. 6.1). Scaling theory assumes usually that the counterion condensation depends only on the Manning parameter $\xi = \ell_B b^{-1} f$ and is hence supposed to be independent of the actual conformation of the chain. Note that the total series B is performed at $\xi = 0.5$ and is thus expected to show no counterion condensation at all according to the standard Manning-Oosawa [44, 45] concept which requires $\xi \geq 1$.

5.3 The Coulomb parameters: ℓ_B and f

As we demonstrated in the previous subsection 5.2, the interplay between counterions and chain conformation influences greatly the behavior of PEs in poor solvent. Therefore also a thorough investigation of the parameters determining the Coulomb interactions is necessary. This section treats the simulation series C1, C2 and C3 where we have investigated the ℓ_B dependence but using different charge fractions $f = 1$ (C1), $f = 1/2$ (C2) and $f = 1/3$ (C3). All simulations are performed at the same charge density ρ_c . We remark that the valences of the charged particles is yet another important independent parameter. But since this is also not included in the scaling picture and would even further complicate the picture we will leave this for another study. We will also look at the behavior of these systems with regard to parameters combined of ℓ_B and f , namely the Manning parameter ξ and the scaling variable $\ell_B b^{-1} f^2$. The Manning parameter is important for the electrostatic field that counterions would experience around a long stretched chain and its value determines in a first approximation the onset of counterion condensation. In the framework of scaling theory simulations performed at the same value of $\ell_B b^{-1} f^2$ should be identical. Nevertheless our simulations show a big difference between the three series. The dependence of R_E on ℓ_B is shown in

fig. 10 and that on n_P in fig. 11. Only for very small val-

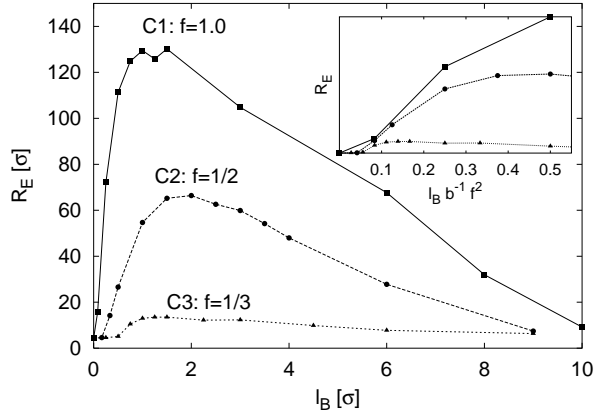


Figure 10. Dependence of R_E on the Bjerrum length ℓ_B for the series C1, C2 and C3. The inlay shows the dependence of R_E on the scaling variable $\ell_B b^{-1} f^2$.

ues of ℓ_B the counterions and their interaction with the chain conformation do not play a significant role. The prediction from scaling theory (see eq. 9) is that our data should collapse on a single master curve. However, our data show that this is only true if the scaling variable $\ell_B b^{-1} f^2$ is smaller than 0.1. This can be seen in the inset in the upper right corner of fig. 10 where we plotted the same data versus $\ell_B b^{-1} f^2$. Upon a further increase of $\ell_B b^{-1} f^2$ the values of the end-to-end distances diverge rapidly. Whereas the chains of series C3 ($f = 1/3$) already start to shrink at $\ell_B b^{-1} f^2 = 0.15$ the chains of the other series still expand.

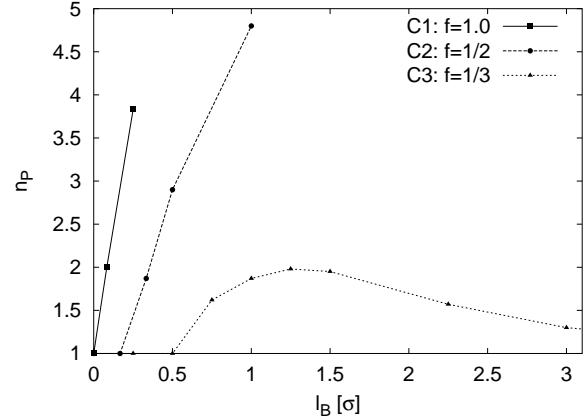


Figure 11. Dependence of n_P on the Bjerrum length ℓ_B for the series C1, C2 and C3.

The different values of f can be seen as different schemes for the discretization of the backbone charge. This has an effect on the correlations between the charges which influences the chain conformation and thus also the counterion distribution. In fig. 12 we have therefore

plotted the integrated counterion distribution $P(r)$ for several values of the Manning parameter ξ for series C2 and C3. Already the curves for $\xi = 0.5$ which corre-

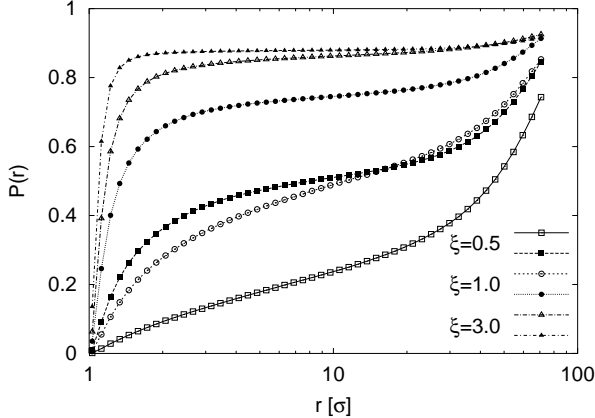


Figure 12. Integrated counterion distribution $P(r)$ around polyelectrolyte chains for different ξ -values. Open symbols show data from series C2 with $f = 1/2$ and filled symbols from C3 with $f = 1/3$.

spond to $\ell_B = 1\sigma$ for series C2 and $\ell_B = 1.5\sigma$ for series C3 show a pronounced difference in $P(r)$. Even though the effect of f on the charge charge correlations may be small it is enhanced strongly by the interplay between the chain conformation and the counterion distribution. When the counterions only slightly move towards the chain due to correlation effects, the effective charge of the chain will shrink and so does the end-to-end distance. A higher effective Manning parameter $\xi_{RE} := Q_Pb/R_E$ follows which again attracts more counterions towards the chain. The same holds for the opposite way. This is the same mechanism which we have already seen for the dependence on ϵ in the previous section. The difference in $P(r)$ becomes smaller with increasing ξ which is due to the gradual collapse of the polyelectrolyte chain, since then in all cases most of the counterions are close or even inside the chains.

In series D we have performed four simulations with $\ell_B b^{-1} f^2 = 0.25$, but different values for ℓ_B and f . In fig. 13 we show the behavior of n_P as a function of ξ . Decreasing f and thus increasing ℓ_B has again a drastic effect on the chain conformation leading to collapse of the chains for large ℓ_B and small f . Even though the number of pearls for the two first points with $f = 1$ and $f = 1/2$ do not differ much the chain extension shows a large difference, namely $R_E = 59\sigma$ for $f = 1$ and $R_E = 32\sigma$ for $f = 1/2$. This is also reflected in a large difference of the pearl sizes and the string lengths. The difference between the systems can again be traced to a quite different distribution of the counterions as can be inspected in fig. 14 where we show $P(r)$ for three of the simulations of series D. It is really surprising that such a small change, basically in the discretization of

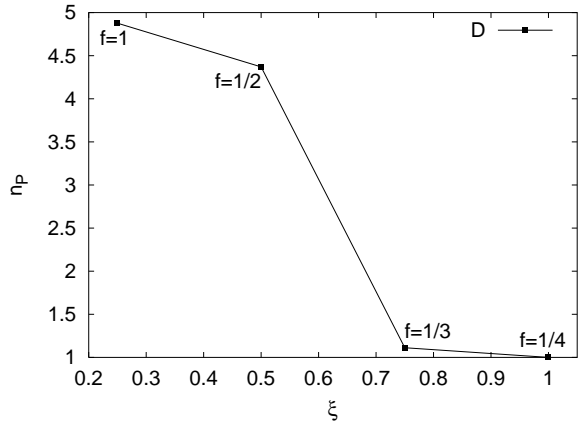


Figure 13. Dependence of n_P on the Manning parameter ξ for the simulation series D with constant scaling parameter $\ell_B b^{-1} f^2 = 0.25$.

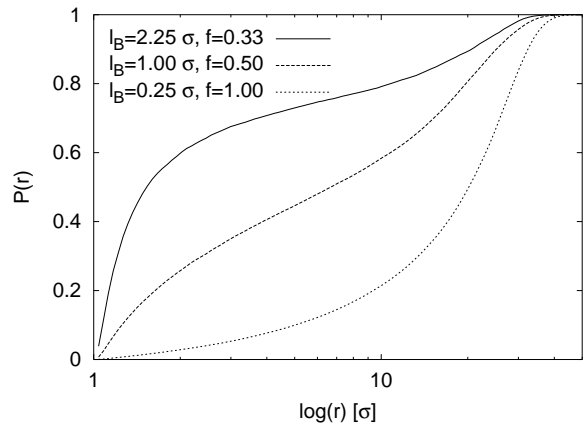


Figure 14. Integrated counterion distributions $P(r)$ are shown for different charge fractions f with constant $\ell_B b^{-1} f^2 = 0.25$ (series D).

the charges, has such a big impact on the chain conformations. This again shows that the delicate balance between repulsive and attractive forces is very sensitive to subtle changes. These effects are definitely not captured by the parameter $\ell_B b^{-1} f^2$ which is used in scaling theories. We will come back to the collapse discussion in sec. 7 where we will also give an overview of the occurring conformations.

6 Fluctuations

The data analysis shows that pearl-necklace conformations are very soft objects which display large fluctuations on all length scales. We will measure in detail the extent of the various fluctuations, since this is important for the interpretation of experimental measurements on polyelectrolyte solutions (see section 8).

6.1 Fluctuations of the structure type - Coexistence

In most of our simulated systems we find coexistence of pearl-necklaces with different number of pearls which we call structure types. It is important to note that the observed coexistence is not caused by frozen meta-stable states. We have excluded this possibility by observing individual chains over a larger period of time each showing a large number of transitions between different structure types during the simulation time. The typical time evolution of the structure type n_P and the radius of gyration R_G for an individual chain is exemplarily shown in fig. 15. In this case the chain mainly fluctuates be-

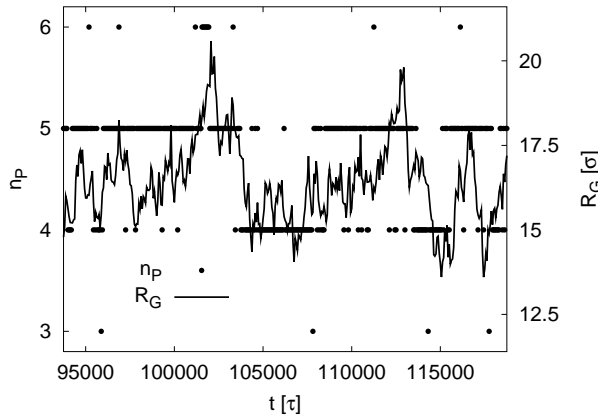


Figure 15. Time evolution of the structure type (number of pearls) and the radius of gyration R_G of a single chain ($N_m = 382$, series A1).

tween structures with 4 and 5 pearls, but we also see a significant fraction of structures with 3 and 6 pearls. Looking at R_G one can see a certain correlation with the structure type which is reflected also in the mean value for different structure types: $R_G^{(3)} = (14.7 \pm 1.3)\sigma$, $R_G^{(4)} = (16.1 \pm 1.5)\sigma$, $R_G^{(5)} = (17.5 \pm 1.6)\sigma$, $R_G^{(6)} = (19.5 \pm 1.7)\sigma$. Here and in the following the superscript denotes that a observable is measured only for conformations with a certain number of pearls n_P . But nevertheless such a simple chain observable is not suited for structural discrimination as one can see from the given mean deviations. The same holds for other chain observables like R_H , the characteristic ratios r and α .

One could be tempted to explain the coexistence of two structure types by a simple finite size argument, namely that the ratio of N_m and the optimal pearl size g_P is not always an integer. In fig. 16 we plot the probability distributions $P(n_P)$ of the structure types for three different chain lengths. We clearly observe a coexistence range containing up to four different structure types. This means that the different observed structure types can only have small differences in the free energy of the order of the thermal fluctuation spectrum. To confirm

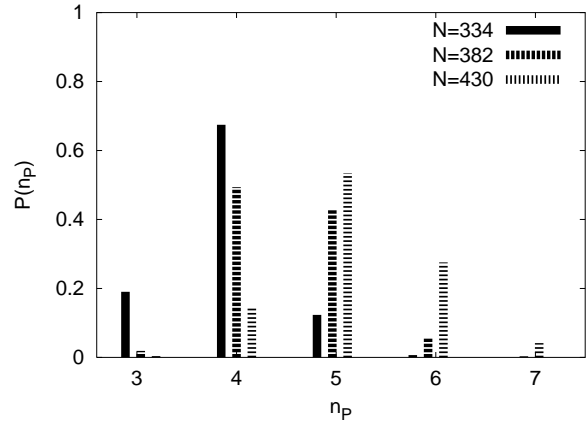


Figure 16. Probability distribution for the structure types found in systems with different chain length from series A1.

this we calculate from the shown probability distribution the free energy differences between structure types with n and m pearls according to the Boltzmann factor:

$$\frac{\Delta \mathcal{F}^{(nm)}}{k_B T} = \frac{\mathcal{F}^{(n)} - \mathcal{F}^{(m)}}{k_B T} = \ln \frac{p^{(n)}}{p^{(m)}} \quad (15)$$

For the case with $N_m = 430$ we find: $\Delta \mathcal{F}^{(45)} = -1.32 k_B T$, $\Delta \mathcal{F}^{(56)} = 0.66 k_B T$, $\Delta \mathcal{F}^{(67)} = 1.9 k_B T$. All values are of the order of $k_B T$ which is consistent with our observed large coexistence regime.

As we will argue these small differences in the free energy between different structure types are mainly due to the interplay of the counterion distribution and the chain conformation. To elucidate the role of the counterions we look at the counterion distribution around the PEs analyzed for each structure type separately. In fig. 17 we have plotted the integrated counterion distributions $P(r)$ for different structure types for the system with $N_m = 430$ from series A1. One observes more counterions to be close to the chains with a smaller pearl number. This can be easily understood if one looks at the far electrostatic field of the chain. For distances larger than the pearl-pearl separation r_{PP} the chain can be seen as a charged cylinder with an effective Manning charge parameter $\xi_{R_E} := Q_P b / R_E$. The end-to-end distance increases with increasing pearl number: $R_E^{(4)} = 48.8\sigma$, $R_E^{(5)} = 54.1\sigma$, $R_E^{(6)} = 60.1\sigma$ and $R_E^{(7)} = 64.0\sigma$, hence the shorter chains have a larger effective Manning charge parameter, namely $\xi_{R_E}^{(4)} = 2.95$, $\xi_{R_E}^{(5)} = 2.67$, $\xi_{R_E}^{(6)} = 2.40$ and $\xi_{R_E}^{(7)} = 2.25$.

Since the PEs in this regime are elongated structures and they carry a large effective line charge it might be worthwhile to compare the ion distribution with predictions from Poisson-Boltzmann (PB) theory. This is also supported by the functional form of the integrated counterion distributions in fig. 17 which looks very sim-

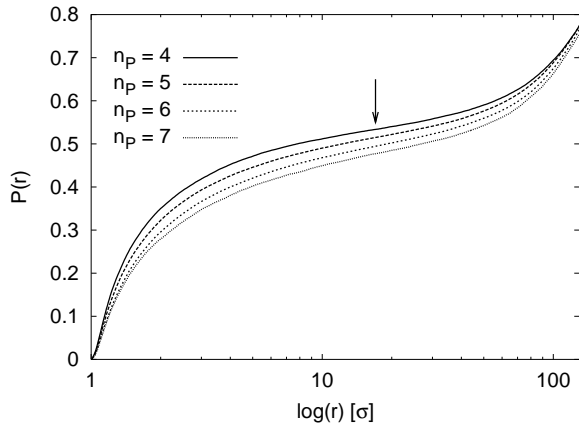


Figure 17. Integrated counterion distributions $P(r)$ for different structure types for the system with $N_m = 430$ from series A1. The arrow pointing to $(17\sigma, 0.53)$ shows the position of the inflection point for the structure type with $n_P = 4$.

ilar to that of an infinitely charged rod within the cell model [46]. In the framework of the PB theory applied to the cell model for an infinitely long charged cylinder [47] one can calculate the fraction f_c of Manning-Oosawa condensed counterions [46, 44, 45] as $f_c = 1 - \frac{1}{\xi}$. In the simulation the fraction of condensed counterions can be read off as the value of $P(r)$ where the $P(r)$ curve, plotted as a function of $\log(r)$, has an inflection point. Using $\xi = \xi_{R_E}$ we find for the $n_P = 4$ structure that the cell model prediction for $f_c = 0.66$ is higher than the value which can be read off the inflection point criterion, that is $f_c = 0.53$. A perfect quantitative agreement can however not be expected since our system is finite, and has as such a smaller electric field, and secondly the pearl-necklace structures do alter the near electrostatic field of the chain and lead to an inhomogeneous counterion distribution. As a word of caution we remark that the bare value for the Manning parameter of the chain in Fig. 17 is 0.5 which would not lead to any counterion condensation at all in the simple Manning picture, and the functional form of an infinite rod with that charge value would simply not show any inflection point. This again demonstrates that poor solvent chains, due to the short range attraction between monomers, feature a higher effective charge density. Since the Poisson-Boltzmann cell model can at least qualitatively explain the change in the counterion distributions a more refined version of this model seems to be necessary. A possible starting point could be to combine the PB rod and sphere geometry as has been suggested in ref. [48].

When more counterions are near the chain we find in terms of a charge renormalization that the effective line charge density of the chain decreases. This allows the chain to contract further which itself induces a stronger counterion attraction. Again a lower effective line charge

density also increases the optimal pearl size. This results in shorter chains with fewer pearls. The opposite, longer chains with more pearls, holds when the counterions move away from the chain. This lowers the difference in the free energy between the different structure types, as was suggested above.

Scaling theories have predicted a collapse of the pearl-necklace structure into a globule as soon as counterion condensation starts [49, 9, 10, 50] due to an avalanche behavior of condensing counterions that contracts the chain. In the investigated parameter range where we observe stable pearl-necklace conformations in our simulation data we did not see such a collapse transition. In the light of a recent study [51] this is not surprising, since it can be shown that this collapse depends on how easily the counterions can enter the globule, the ion concentration, and the strength of the electrostatic interaction. Also the necessary amount of condensed counterions to induce the collapse can be quite high.

We also suggest that the fluctuations due to the presence of the counterions lower the energy barrier between the different structure types. To confirm this suggestion one would need to analyze the transition frequency between the different structure types for chains with explicit counterions and a corresponding Debye-Hückel chain with the same n_P . This is however outside the scope of the present investigations.

6.2 Fluctuations of the substructures

In this section we discuss fluctuations of the chain conformation on a smaller length scale, namely the radius of the pearls r_P and the pearl-pearl distance r_{PP} . The probability distributions for the pearl size g_P is shown in fig. 18 and for the pearl-pearl distance r_{PP} in fig. 19.

Both distributions are quite broad. The relative standard deviations for the distributions of all chains are $\delta g_P = 0.32$ and $\delta r_{PP} = 0.22$.

As we have already seen for the overall chain extension also the size of the substructures are influenced by the counterion distribution. The pearl size is decreasing with increasing number of pearls and increasing chain extension as one can see from the arrows in fig. 18. Still an explanation in terms of a charge renormalization is not sufficient for an understanding. This becomes more clear when we look at the number of counterions inside a shell around the chains. Rounded to integers we find for a shell radius of 3σ on average 56 counterions. Averaged separately for the different structure types we find 60, 57, 53 and 50 counterions for structures with 4, 5, 6 and 7 pearls. It is interesting to note, that the difference in this number of counterions is roughly constant for shells with radii ranging from 2σ up to 30σ and is thus independent of the exact definition of counterions called “condensed” to the chains. Thus we now use a practical definition of an effective charge using the counterions which are closer than 3σ to the next monomer. For the

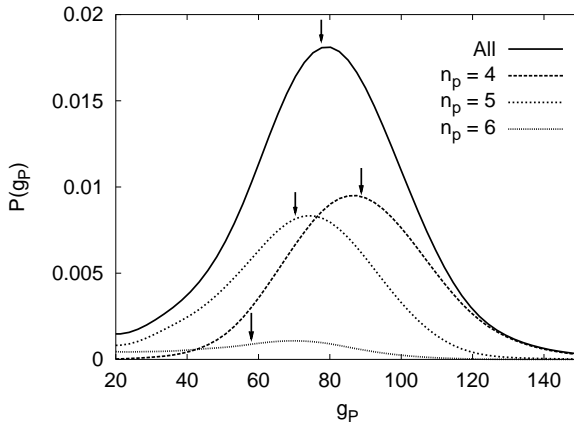


Figure 18. Probability distributions P for the pearl size g_P for the system with chain length $N_m = 382$ from series A1. Shown is the distribution for all chains as well as the distributions for the different structure types. The arrows mark the mean value of the corresponding probability distribution.

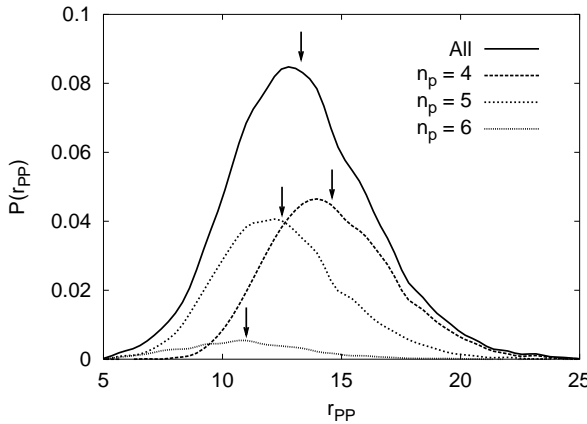


Figure 19. Probability distributions P for the pearl-pearl distance r_{PP} for the system with chain length $N_m = 382$ from series A1. Shown is the distribution for all chains as well as the distributions for the different structure types. The arrows mark the mean value of the corresponding probability distribution.

example this yields an effective pearl charge of 18, 15, 13 and 11 charges for structures with 4, 5, 6 and 7 pearls respectively. Since the pearl size is only slowly varying one gets large differences in the electrostatic self energy of the pearls of different structure types.

In the scaling Ansatz the distance between neighboring pearls r_{PP} is determined by the balance between the electrostatic repulsion between the chains and the energy one needs to pull monomers out of the pearls. The second term is related to the surface tension and is roughly constant. The term connected to electrostatics

is more complex. We approximate it by the electrostatic energy of two point charges carrying the average pearl charge, separated by the average pearl-pearl distance. r_{PP} ranges from 15.4σ for 4-pearl structures to 11.1σ for 7-pearl structures. Together with the above calculated effective pearl charges we can estimate the electrostatic repulsion between neighboring pearls to be $31.9k_B T$ for 4-pearl structures and $16.7k_B T$ for 7-pearl structures. Note that we neglect the energetic contribution of the other pearls. This difference can also not be explained by a standard Debye-Hückel potential since the Debye screening length, calculated from the bulk charge density $\rho_c = 1 \times 10^{-5}\sigma^{-3}$ in the system, is $\lambda_D = 72.8\sigma$ and is thus much larger than the values for r_{PP} . Of course, closer to the chain the counterion density is much larger than in the bulk which could be a hint to explain the observed differences. The counterion density is rapidly varying with the distance from the chain starting with $\approx \times 10^{-1}\sigma^{-3}$ at a distance of 1.5σ and dropping below the bulk density at a distance of 50σ .

The electrostatic self energy of the pearls and the electrostatic pearl-pearl repulsion show explicitly the discrepancies between a mean field approach and our simulational results. It also clearly demonstrates that it is necessary to include the counterion distribution into the model. Moreover correlations between the counterions and the chain charges seem to play an important role. For instance, it can be shown that the counterions preferentially accumulate between the pearls. Since the structure of polyelectrolytes in poor solvent turns out to be extremely sensitive to the inhomogeneities of the counterion distribution it should be used as a test case for the development of theoretical approaches beyond the mean field level. A more detailed discussion of these inhomogeneities can be found in ref. [21, 52]

7 The sausage regime and phase space

In order to get an overview of the parameter regimes our different simulation series are scanning through we have depicted them in a phase plot for polyelectrolytes using the parameters ϵ and ℓ_B^{-1} as it was done for example in Ref. [10]. Some of the simulation series are marked with dashed lines in fig. 20. Close to the lines we have put some snapshots of the configurations to get a visual impression.

Looking at series C3 crossing the entire ℓ_B -range we find, starting on the right side at the neutral case with $\ell_B = 0.0\sigma$, a neutral globule. The chain is collapsed due to the poor solvent. With increasing ℓ_B the chain is getting charged, the self-energy grows, and we can observe the Rayleigh instability at $\ell_B = 0.75\sigma$ where the globule splits into a dumbbell. At this point we find already some counterions close to the chain, hence there are condensed counterions present. Further increase of ℓ_B can lead to further Rayleigh instabilities, depending on the parameters. Then, after reaching its maximum

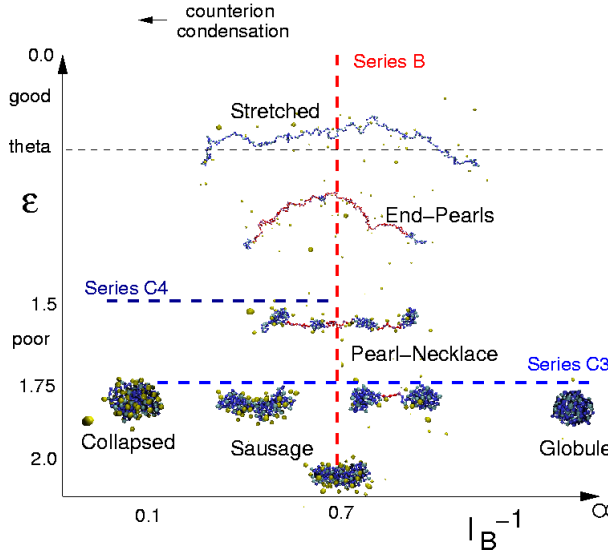


Figure 20. Schematic view of the location of the different PE configuration types in the ϵ/ℓ_B^{-1} phase diagram. All simulations are performed at $f = \frac{1}{3}$. The dashed lines indicate the location of the simulation series B, C3 and C4.

extension at $\ell_B = 1.25\sigma$ the chain slowly shrinks, since the enlarged Coulomb repulsion gets overcompensated by condensing counterions. Finally we reach a collapsed conformation at $\ell_B = 9.0\sigma$. The non-monotonic behavior of the chain extension is qualitatively the same as in the good solvent case and qualitatively well understood [10, 53, 54]; however, the decrease is faster and more pronounced in the poor solvent case [19, 55].

Scaling theories have predicted that with the onset of condensation the pearl-necklace should collapse in a first-order transition [49, 9, 10, 50]. However we find always a smooth distribution of counterions which looks like a distribution that can be calculated within PB theory [43]. The counterions get pulled closer to the macroion as the Coulomb coupling is increased, and a rather high Bjerrum length, or similarly, a large number of condensed counterions are needed to collapse the PE to a globule. Also the osmotic pressure does not show any dramatic decrease with ℓ_B , so we believe that for an adequate description of the collapse we need a refined theory.

A very interesting, and as we believe, new conformational regime opens up basically for those ℓ_B values between the maximal chain extension up to the collapsed state. Here we find conformations that are reminiscent of a cigar-like shape [49], but turn out to look more like a sausage for longer chains. Since with increasing ℓ_B more counterions are attracted towards the chain the pearl-pearl repulsion is getting screened such that the pearls slowly coalesce and the conformation is not stretched on longer length scales anymore. Due to its shape we have termed it the sausage regime. Note that the actual con-

formation depends also on f where smaller values of f lead to thicker sausages. Conformational snapshots are shown in fig. 21.

At the crossing point of series B and C3 at $f = \frac{1}{3}$, $\ell_B = 1.5\sigma$ and $\epsilon = 1.75k_B T$ being in the pearl-necklace regime, we have studied the N_m -dependence of the chain conformation. Starting from short chains which form a globule, e.g. one pearl, we enter a number of Rayleigh instabilities upon elongation. A few exemplary snapshots of series A1 have already been shown in fig. 4.

As a next step we have studied the dependence of the conformations upon the charge fraction f . As one can see in fig. 21 this opens up a completely new plane in the phase diagram of polyelectrolytes. The three simulation series C1, C2 and C3 all scan the entire ℓ_B -range and differ only in the charge fraction f .

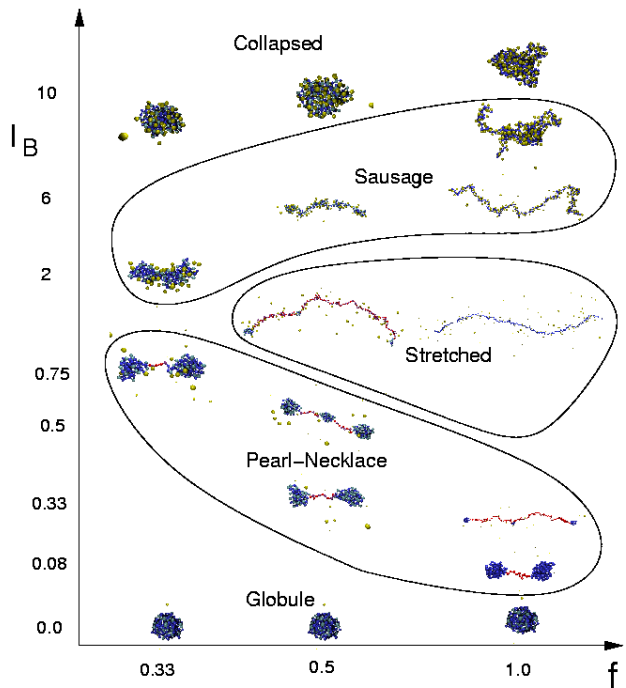


Figure 21. Schematic view of the location of the different PE configuration types in the ℓ_B/f phase diagram. The simulations are from series C1 at $f = 1$, C2 at $f = \frac{1}{2}$ and C3 at $f = \frac{1}{3}$ performed at $\epsilon = 1.75k_B T$.

In mean field theories for polyelectrolytes we find two important parameters. The first one is the Manning parameter $\xi = \ell_B b^{-1} f$ which plays a role in all attempts to renormalize the charge of highly charged polyelectrolytes [44]. The second one is a measure for the overall Coulombic repulsion on a charged chain $\ell_B b^{-1} f^2$. As a first Ansatz for a scaling theory for highly charged polyelectrolytes at finite density an effective charge fraction $f_{\text{eff}} = \frac{f}{\xi}$ is often used, trying to combine both parameters. In this framework the three simulation series should behave identically. In contrast to this we find e.g. that the maximal extension $R_E(\text{max})$ for the three series dif-

fers strongly. Namely we find for C1 $R_{\text{E(max)}} = 130\sigma$, for C2 $R_{\text{E(max)}} = 66.4\sigma$ and for C3 $R_{\text{E(max)}} = 13.5\sigma$. It is also striking that only the series with larger f has a regime where the chains are stretched and they behave as if they were in a good solvent.

The Rayleigh instability occurs at the same value $\ell_B b^{-1} f^2 \approx 1/12$ for all three series as expected because the counterions do not play a dominant role here. Increasing ℓ_B from this point on the three series behave very differently. Whereas the series with $f = \frac{1}{2}$ and $f = 1$ show a cascade of Rayleigh instabilities budding more pearls until they reach stretched conformations the series with $f = \frac{1}{3}$ has a dumbbell conformation at the maximum extension. The maximum extension itself is reached at different values for ℓ_B (see fig. 10). For series C1 the maximum extension is probably more restricted by the chain entropy than that is determined by the interplay between repulsive and attractive interactions. The chains then slowly shrink and enter the sausage regime. Still at the same value of ℓ_B the chains with $f = 1$ are much longer than the chains with $f = \frac{1}{2}$ or $f = \frac{1}{3}$. Finally the collapsed conformation is reached roughly at the same value of $\ell_B \approx 8\sigma$. In this regime we have almost a dense electrolyte solution with mobile ions inside the chains so we should be close to the critical behavior of a Coulomb fluid. This suggest that the collapse should occur at roughly the same value of the coupling parameter $v_m v_c \ell_B / \sigma$ which is the interaction energy of two oppositely charged ions at contact in units of $k_B T$. In principle the phase space for polyelectrolytes has far more than the shown three dimensions. As we know from previous studies [19, 36, 22, 24, 23] also the density is a very relevant parameter and would have to be included into the phase diagram. Further important parameters are the valency of the counterions, and added salt concentrations which we did not investigate at all here. This all reflects the fact that there is presumably no general parameter for the Coulomb interaction.

8 Chain conformation and experiments

The last section focuses on the connection between the chain conformation and experimentally accessible observables like the characteristic ratios r and α and the form factor S_1 .

8.1 Characteristic ratios

The characteristic ratios $r = (R_{\text{E}}/R_{\text{G}})^2$ and $\alpha = R_{\text{G}}/R_{\text{H}}$ are often used as a first step to characterize conformations that are extended in one dimension. Since both R_{G} and R_{H} are accessible with experimental methods it is interesting to know how α can be used to distinguish different conformation types.

In fig. 22 and fig. 23 we show the change of the characteristic ratios r and α with ℓ_B for the series C1, C2 and C3, e.g. for different f . For the globular conformation at

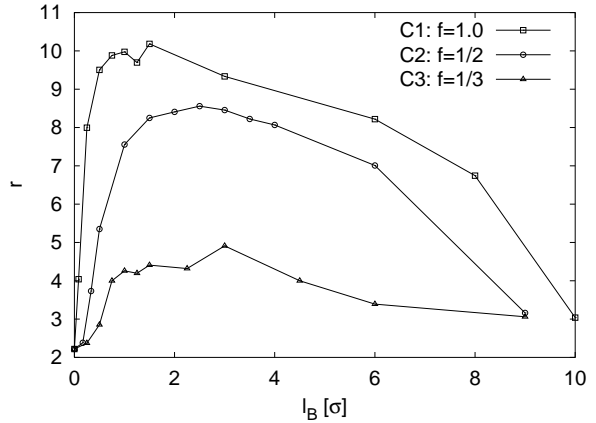


Figure 22. Change of the characteristic ratio r with ℓ_B for different f (series C1, C2 and C3).

$\ell_B = 0\sigma$ we find $r \approx 2.2$ and $\alpha \approx 0.9$. For dumbbells we find values for r between 4 and 4.5 and $\alpha \approx 1.6$. With further increase of ℓ_B both observables reach a maximum roughly at the maximal chain extension (compare to fig 10). Then r and α decrease monotonically until the collapsed conformation is reached at high values of ℓ_B where we find $r \approx 3$ and $\alpha \approx 1$. For a globular object one can calculate r to be between 2 and $10/3$ which is consistent with our findings. For a completely stretched object one would have $r = 12$ which is of course not reached with the simulations. The form of the shown

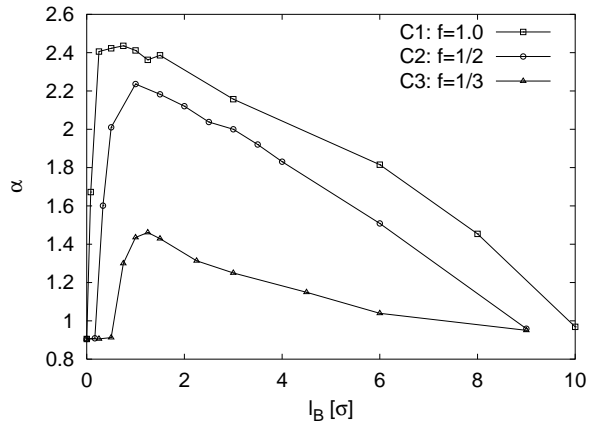


Figure 23. Change of the characteristic ratio α with ℓ_B for different f (series C1, C2 and C3).

curves for r and α clearly indicates that it is not possible to deduce the conformation type since at each value the chain could either be in a pearl-necklace conformation or, at higher ℓ_B in a sausage like conformation. Since for the pearl-necklace regime itself α is a monotonic function of n_P we have plotted the values of α for all simulations in this paper that we assign to this regime in fig. 24. One can see a clear jump of α between $n_P = 1$

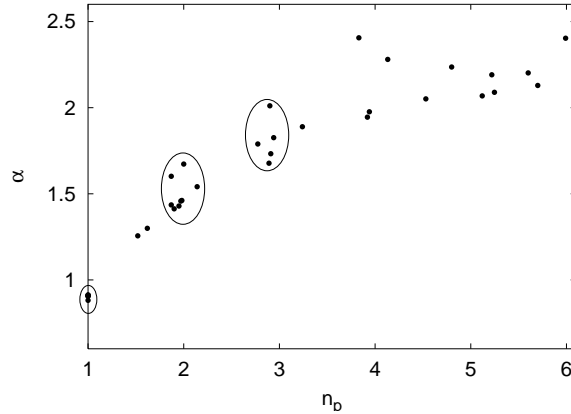


Figure 24. Characteristic ratio α for pearl-necklace structures as function of n_P . The ellipses combine points close to $n_P = 1, 2$ and 3 .

and $n_P = 2$. But the range of α between conformations with two and three pearls are already overlapping. With increasing n_P the slope of $\alpha(n_P)$ is decreasing and a further structure discrimination is not possible. So even in the pearl-necklace regime it is problematic to use α to discriminate pearl-necklace conformations with different numbers of pearls.

8.2 Form factor

More information about the chain conformation is contained in the form factor S_1 (see eq. 5). In fig. 25 we show $S_1(q)$ for different simulations from series C2. The figure shows the form factors for the different conformation types we have found in our simulations, namely the neutral globule, the dumbbell, the three pearl conformation, stretched chains, sausage like conformations and a collapsed chain with most of the counterions being inside. The neutral globule shows Porod scattering. The strong oscillations show that the globule has sharp boundaries and does not fluctuate strongly. $S_1(q)$ for the dumbbell exhibits a shoulder at $q \approx 0.5\sigma^{-1}$ corresponding to a length of $\approx 12.5\sigma$ that can be identified as the distance between the two pearls. The strong decrease at higher q -values indicates again a Porod scattering in this case coming from the surface of the pearls. The minima of the Porod scattering are smeared out by fluctuations of the shape and size of the pearls. For the three pearl conformations we find two shoulders one at $q \approx 0.2\sigma^{-1}$ and one at $q \approx 0.4\sigma^{-1}$. They are also indications of the pearl-pearl distances. But the shoulders here are already less pronounced than in the case of the dumbbell. The stretched conformation has a qualitative different $S_1(q)$ showing a scaling with q^{-1} over a large q -range. It follows that the chain is stretched on length scales larger than 10σ up to its full length of 66σ . For the sausage like conformation we can not identify

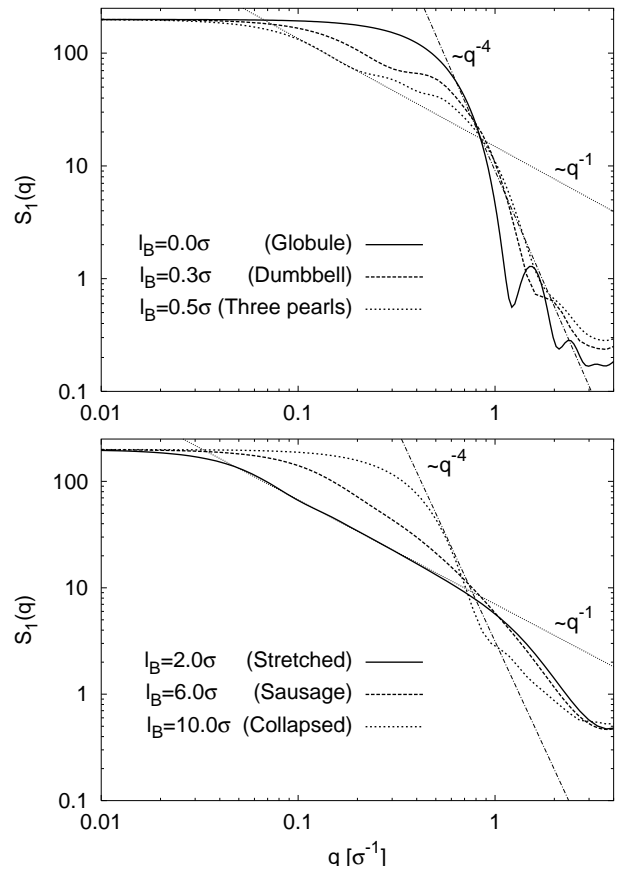


Figure 25. Form factors for the different conformation types while changing ℓ_B for series C2. The straight lines indicate a stretched chain with $S_1 \propto q^{-1}$ and Porod scattering with $S_1 \propto q^{-4}$.

any scaling regime or other signatures. Thus we can not obtain another length scale than the overall chain extension. The collapsed globule shows again, like the neutral globule, a strong decrease of the scattering intensity at large q -values. The rudimentary observable Porod scattering is strongly smeared out showing that the competition between attractive and repulsive forces induces large fluctuations on the surface of the globular object.

After this overview over the scattering of the different conformation types we discuss the form factor of pearl-necklace conformations with a larger number of pearls in more detail. In this case the scattering is not only influenced by the fluctuations in shape and size of the pearls and strings but also by the fluctuations of the structure type, namely different numbers of pearls. The form factor shows four different regimes which reassemble the different length scales that are involved in a pearl-necklace structure. For chains taken from series A1 with $N_m = 382$ the form factor is plotted in fig. 26. In the Guinnier regime at $R_G q \ll 1$ the radius of gyration R_G can be calculated from $S_1(q) = N_m (1 - (R_G q)^2/3)$.

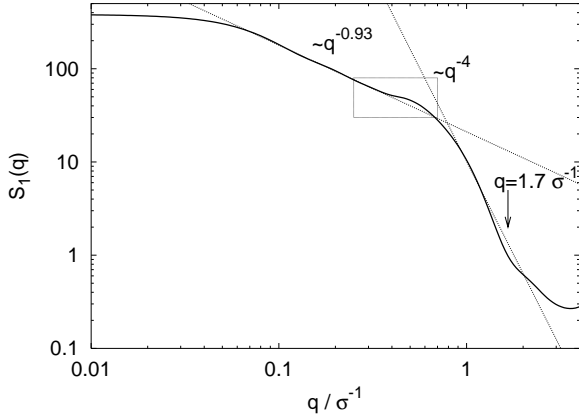


Figure 26. Form factor S_1 for typical pearl-necklace conformations. The dotted lines are fits to certain q ranges, see text. The marked region is enlarged in fig. 27. The chains have a length $N_m = 382$ and on average $n_P = 4.5$ pearls.

This yields $R_G = 16.8\sigma \pm 0.3\sigma$ in good agreement with the directly calculated value $R_G = 16.9\sigma \pm 0.4\sigma$. In the following range $0.07\sigma^{-1} \leq q \leq 0.4\sigma^{-1}$ the single chain structure factor scales as $S_1(q) \propto q^{-1}$. The chain conformations are thus stretched on length scales larger than 15σ . At $q \approx 0.5\sigma^{-1}$ one can see a weakly pronounced shoulder in S_1 . A closer look to this region reveals that $S_1(q)$ has an inflection point at $q = 0.46\sigma^{-1}$ which is shown in fig. 27. A comparison with the in-

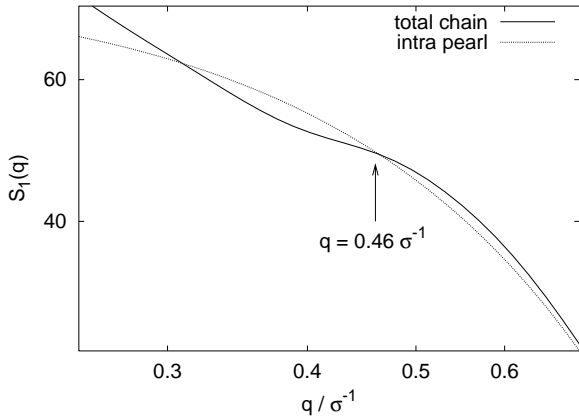


Figure 27. The pearl-pearl distance leaves only a very small signature in the form factor as can be seen in the close view of a comparison of the total form factor and the intra pearl form factor.

tra pearl scattering shows that this is due to inter pearl scattering. This becomes more clear when one looks at the analytic scattering function S_a of a linear arrangement of n homogenous spheres with a diameter r_P and a distance r_{PP} . S_a is the product of the inter pearl scat-

tering S_{inter} and the intra pearl scattering S_{intra} . The inter pearl scattering is given by

$$S_{\text{inter}} = n + 2 \sum_{k=1}^{n-1} (n-k) \frac{\sin(qr_{PP}k)}{qr_{PP}k}. \quad (16)$$

The intra pearl scattering is that of a homogenous sphere and thus given by the Porod scattering:

$$S_{\text{intra}} = \frac{\sin(qr_P) - qr_P \cos(qr_P)}{qr_P^3} \quad (17)$$

Dividing out the intra pearl scattering from S_1 gives access to the inter pearl scattering and thus r_{PP} . From the inflection point in the inter pearl scattering one can calculate the pearl pearl distance. This yields $r_{PP} = 13.6\sigma$, again in accord with the directly measured value $r_{PP} = 13.3\sigma$. In the high q -range between $q \approx 0.9\sigma^{-1}$ and $q \approx 2.5\sigma^{-1}$ we find $S_1(q) \propto q^{-4}$, the typical Porod scattering with a small dip at $q \approx 1.7\sigma^{-1}$. Fitting the data to eq. 17 yields a pearl radius $r_P \approx 2.6\sigma$ which again compares well to the directly calculated value $r_P \approx 3.0\sigma$. We conclude that the cooperative effect of fluctuations on overlapping length scales broadens all characteristic signatures which can be revealed by scattering under experimental conditions like polydispersity and line charge density fluctuations. Thus necklaces might be difficult to detect. We find the most pronounced necklace signatures for the dumbbell conformation.

9 Conclusion

We have studied a dilute solution of strongly charged polyelectrolytes in a poor solvent by means of molecular dynamics simulations for a variety of different parameters.

We have developed a cluster algorithm to characterize pearl-necklace structures even for single configurations and performed an extensive data analysis of all the pearl-necklace conformations in our simulations.

We found that the range where scaling predictions are applicable is confined to a small range of parameters. One either has to stay close to the infinite dilution limit or use weakly charged chains to exclude counterion effects. The reason is that even in a dilute solution there is already a delicate interplay between the counterion distribution and the chain conformation for strongly charged chains. This became in particular evident in our investigations studying the dependence on the solvent quality and the Coulomb parameters ℓ_B and f .

Our results challenge approaches that apply Manning-like charge renormalization and simple scaling concepts to strongly charged polyelectrolytes. Since we found strong effects already for dilute solutions we expect an even more complicated counterion chain coupling for semi-dilute and dense polyelectrolyte solutions.

We have discussed the different types of fluctuations present for pearl-necklace structures and quantified them

for our data. We showed that the free energy differences between the structure types can be very small and that the size and position of the substructures exhibit large fluctuations.

In a preliminary classification of the phase space of PEs in poor solvent we have shown that the phase space is multi-dimensional and that the region for pearl-necklace structures is rather small. In this context we have also investigated the Coulomb induced collapse of poor solvent PEs which appears to be a rather smooth transition. There we have shown that the strong screening in the vicinity of the charged chains leads to sausage like conformations instead of pearl-necklaces. Our data suggest that the collapse is determined by the Bjerrum length since it occurs at $\ell_B \approx 8\sigma$ for all systems which lead us to suggest that in the collapsed state ion-ion correlations $\propto \ell_B$ play the most prominent part.

Finally we computed some experimentally accessible observables like the form factor and characteristic size ratios. This should help to analyze the experimental data and to discover pearl-necklace signatures which, according to our understanding, are not very pronounced.

10 Acknowledgments

We thank K. Kremer, B. Dünweg, B. Mergell, H. Schiessel and M. N. Tamashiro for many fruitful discussions and comments. We also want to thank R. Everaers for contributions to the cluster algorithm. We gratefully acknowledge partial funding by the DFG SPP 1009 and SFB 625, and through the “Zentrum für Multifunktionelle Werkstoffe und Miniaturisierte Funktionseinheiten”, grant BMBF 03N 6500.

References and Notes

- (1) Barrat, J.-L.; Joanny, J.-F. *Advances in Chemical Physics* **1996**, *94*, 1–66.
- (2) Hara, M., Ed. *Polyelectrolytes: Science and Technology*; Marcel Dekker: New York, 1993.
- (3) Schmitz, K. S. *Macroions in solution and colloidal suspension*; VCH Publishers: New York, 1 ed., 1993.
- (4) Förster, S.; Schmidt, M. *Advances in Polymer Science* **1995**, *120*, 51–133.
- (5) Holm, C., Kékicheff, P., Podgornik, R., Eds. *Electrostatic Effects in Soft Matter and Biophysics*, Vol. 46 of *NATO Science Series II - Mathematics, Physics and Chemistry*; Kluwer Academic Publishers: Dordrecht, NL, 2001.
- (6) K.P.Ghiggino.; K.L.Tan. In *Polymer photophysics*; Phillips, D., Ed.; Chapman and Hall: London; New York, 1985; chapter 7, pages 341–375.
- (7) Kantor, Y.; Kardar, M.; Li, H. *Phys. Rev.* **1994**, *E49*, 1383.
- (8) Kantor, Y.; Kardar, M. *Phys. Rev. E* **1995**, *51*, 1299.
- (9) Dobrynin, A. V.; Rubinstein, M.; Obukhov, S. P. *Macromolecules* **1996**, *29*(8), 2974.
- (10) Schiessel, H.; Pincus, P. *Macromolecules* **1998**, *31*, 7953–7959.
- (11) Schiessel, H. *Macromolecules* **1999**, *32*, 5673–5680.
- (12) Dobrynin, A. V.; Rubinstein, M. *Macromolecules* **1999**, *32*(3), 915–922.
- (13) Dobrynin, A. V.; Rubinstein, M. *Macromolecules* **2001**, *34*(6), 1964–1972.
- (14) Solis, F. J.; de la Cruz, M. O. *Macromolecules* **1998**, *31*(16), 5502–5506.
- (15) Pickett, G. T.; Balazs, A. C. *Langmuir* **2001**, *17*(16), 5111–5117.
- (16) Migliorini, G.; Lee, N.; Rostishvili, V.; Vilgis, T. A. *European Physical Journal E* **2001**, *6*(3), 259–270.
- (17) Lyulin, A. V.; Dünweg, B.; Borisov, O. V.; Darinskii, A. A. *Macromolecules* **1999**, *32*(10), 3264–3278.
- (18) Chodanowski, P.; Stoll, S. *J. Chem. Phys.* **1999**, *111*(13), 6069–6081.
- (19) Micka, U.; Holm, C.; Kremer, K. *Langmuir* **1999**, *15*, 4033.
- (20) Micka, U.; Kremer, K. *Europhys. Lett.* **2000**, *49*(2), 189–195.
- (21) Limbach, H. J.; Holm, C. *J. Chem. Phys.* **2001**, *114*(21), 9674–9682.
- (22) Limbach, H. J.; Holm, C. *Comp. Phys. Comp.* **2002**, *147*, 321–324.
- (23) Holm, C.; Limbach, H. J.; Kremer, K. *J. Phys.: Condens. Matter* **2003**, *15*, S205–S211.
- (24) Limbach, H.; Holm, C.; Kremer, K. *Europhys. Lett.* **2002**, *60*(4), 566–572.
- (25) Spiteri, M. N.; Boue, F.; Lapp, A.; Cotton, J. P. *Physica B* **1997**, *234*, 303–305.
- (26) Carballo-Tinoco, M. D.; Williams, C. E. *Europhys. Lett.* **2000**, *52*(3), 284–290.
- (27) Heinrich, M.; Rawiso, M.; Zilliox, J. G.; Lesieur, P.; Simon, J. P. *Eur. Phys. J. E* **2001**, *4*(2), 131–142.

(28) Aseyev, V. O.; Klenin, S. I.; Tenhu, H.; Grillo, I.; Geissler, E. *Macromolecules* **2001**, *34*(11), 3706–3709.

(29) Minko, S.; Kiriy, A.; Gorodyska, G.; Stamm, M. *J. Am. Chem. Soc.* **2002**, *124*(13), 3218–3219.

(30) Lee, M.-J.; Green, M. M.; Mikes, F.; Morawetz, H. *Macromolecules* **2002**, *35*(10), 4216–4217.

(31) de Gennes, P.; Pincus, P.; Velasco, R. *J. Physique* **1976**, *37*, 1461.

(32) Essafi, W.; Lafuma, F.; Williams, C. E. *J. Phys. II* **1995**, *5*, 1269–1275.

(33) Heitz, C.; Rawiso, M.; François, J. *Polymer* **1999**, *40*(7), 1637–1650.

(34) Waigh, T. A.; Ober, R.; Williams, C. E.; Galin, J.-C. *Macromolecules* **2001**, *34*(6), 1973–1980.

(35) Baigl, D.; Williams, C. E. *privat communication, to be published* **2002**.

(36) Limbach, H. J. *Struktur und Eigenschaften von Polyelektrolyten im schlechten Lösungsmittel* PhD thesis, Johannes Gutenberg Universität, Mainz, Germany, **2001**.

(37) Deserno, M.; Holm, C. *J. Chem. Phys.* **1998**, *109*, 7678.

(38) Deserno, M.; Holm, C. *J. Chem. Phys.* **1998**, *109*, 7694.

(39) Grest, G. S.; Kremer, K. *Phys. Rev. A* **1986**, *33*(5), 3628–31.

(40) Liu, B.; Dünweg, B. *J. Chem. Phys.* **2003**, *118*(17), 8061–8072.

(41) Schweins, R.; Huber, K. *Eur. Phys. J. E* **2001**, *E* 5, 117–126.

(42) Belloni, L. *Colloids and Surfaces* **1998**, *A* 140, 227.

(43) Deserno, M.; Holm, C.; May, S. *Macromolecules* **2000**, *33*, 199–206.

(44) Manning, G. *J. Chem. Phys.* **1969**, *51*, 924–933.

(45) Oosawa, F. *Polyelectrolytes*; Marcel Dekker: New York, 1971.

(46) Deserno, M. *Counterion condensation for rigid linear polyelectrolytes* PhD thesis, Universität Mainz, **2000**.

(47) Deserno, M.; Holm, C. In *Electrostatic effects in Soft Matter and Biophysics*; Holm, C., Kékicheff, P., Podgornik, R., Eds.; Kluwer Academic Publishers: Dordrecht, NL, 2001; Vol. 46 of *NATO Science Series II - Mathematics, Physics and Chemistry*.

(48) Deshkovski, A.; Obukhov, S.; Rubinstein, M. *Phys. Rev. Lett.* **2001**, *86*(11), 2341–2344.

(49) Khokhlov, A. *J. Phys. A* **1980**, *13*, 979.

(50) Vilgis, T. A.; Johner, A.; Joanny, J.-F. *Eur. Phys. J. E* **2000**, *2*(3), 289–300.

(51) Deserno, M. *Eur. Phys. J. E* **2001**, *6*, 163–168.

(52) Castelnovo, M.; Sens, P.; Joanny, J.-F. *Eur. Phys. J. E* **2000**, *1*, 115–125.

(53) Stevens, M. J.; Kremer, K. *J. Chem. Phys.* **1995**, *103*(4), 1669–1690.

(54) Winkler, R. G.; Gold, M.; Reineker, P. *Phys. Rev. Lett.* **1997**, *80*, 3731–3734.

(55) Khan, M.; Jönsson, B. *Biopolymers* **1999**, *49*, 121.

A Simulated Systems

Here we give a detailed overview over the parameters of the simulated systems and some basic observables, namely the chain length N_m , the end-to-end distance R_E , the hydrodynamic radius R_H , the characteristic ratios $r = (R_E/R_G)^2$ and $\alpha = R_G/R_H$ and the osmotic coefficient $OC = \Pi/p_{ig}$, where Π is the pressure and p_{ig} is the ideal gas pressure. If possible, also the number of pearls n_P and the average number of monomers in a pearl g_P is given. In the tables 1 to 9 R_E , R_H and ℓ_B are given in σ , ϵ in $k_B T$. All other quantities in the tables are dimensionless numbers. The statistical error for the chain extensions R_E and R_H is smaller than 10%. g_P exhibits a systematic error of ± 4 monomers. For $g_P > 30$ the number of pearls has an accuracy of $\approx 5\%$. For smaller g_P values this error becomes larger. The statistical error of the pressure calculation gives rise to an error of the osmotic coefficient of ± 0.06 resulting in a large relative error for small values of OC .

TABLE 1: Series A1: $N_m = 48\ldots478$, $\epsilon = 1.75k_B T$, $\ell_B = 1.5\sigma$, $f = 1/3$, $\rho_c = 1.0 \times 10^{-5}\sigma^{-3}$

N_m	R_E	R_H	r	α	n_P	g_P	OC
48	3.48	2.19	3.25	0.88	1.00	46.0	0.96
94	4.56	2.71	3.40	0.91	1.01	93.9	0.68
142	12.9	4.11	4.63	1.46	1.97	68.8	0.60
190	15.0	4.60	4.49	1.54	2.01	90.4	0.44
238	25.7	5.86	5.84	1.83	2.94	75.5	0.46
286	30.4	6.51	6.10	1.89	3.24	82.5	0.42
334	38.2	7.44	6.73	1.98	3.94	78.6	0.40
382	45.4	8.24	7.24	2.05	4.53	78.0	0.35
430	55.4	9.22	7.55	2.19	5.22	75.2	0.36
478	59.7	9.81	7.61	2.20	5.60	78.3	0.39

TABLE 2: Series A2: $N_m = 100\ldots300$, $\epsilon = 1.75k_B T$, $\ell_B = 1.5\sigma$, $f = 1/2$, $\rho_c = 6.7 \times 10^{-5}\sigma^{-3}$

N_m	R_E	R_H	r	α	np	g_P	OC
99	26.8	5.59	7.17	1.79	2.77	23.3	0.54
199	68.1	10.43	8.20	2.28	4.13	20.7	0.32
299	102.9	14.37	8.88	2.40	5.99	18.9	0.39

TABLE 3: Series A3: $N_m = 100\ldots300$, $\epsilon = 1.75k_B T$, $\ell_B = 1.5\sigma$, $f = 1/2$, $\rho_c = 6.7 \times 10^{-5}\sigma^{-3}$

N_m	R_E	R_H	r	α	np	g_P	OC
99	22.1	5.08	6.72	1.68	2.89	25.1	0.46
199	54.9	9.15	8.24	2.09	5.25	21.4	0.36
299	83.4	12.6	8.69	2.24	7.68	20.4	0.35

TABLE 4: Series B: $\epsilon = 0.0k_B T\ldots2.0k_B T$, $N_m = 238$, $\ell_B = 1.5\sigma$, $f = 1/3$, $\rho_c = 5.0 \times 10^{-5}\sigma^{-3}$

ϵ	R_E	R_H	r	α	np	g_P	OC
0.00	102	16.2	8.88	2.11	—	—	0.66
0.50	100	14.9	9.28	2.21	—	—	0.62
1.00	82.2	13.1	8.81	2.11	—	—	0.63
1.25	68.7	11.0	8.44	2.15	—	—	0.53
1.35	58.5	9.78	7.91	2.13	5.70	25.2	0.52
1.45	45.9	8.22	7.32	2.07	5.12	35.6	0.53
1.55	34.3	6.89	6.56	1.94	3.92	52.9	0.45
1.65	24.2	5.83	5.76	1.73	2.91	76.8	0.48
1.75	16.8	5.03	4.72	1.54	2.14	108	0.36
1.85	13.8	4.68	4.36	1.41	1.90	123	0.31
2.00	11.2	4.34	4.21	1.26	1.52	155	0.26

TABLE 5: Series C1: $\ell_B = 0.0\ldots12.0\sigma$, $f = 1$, $\epsilon = 1.75k_B T$, $N_m = 200$, $\rho_c = 5.0 \times 10^{-5}\sigma^{-3}$

ℓ_B	R_E	R_H	r	α	np	g_P	OC
0.0	4.41	3.27	2.22	0.91	1.0	200	0.97
0.083	15.8	4.70	4.04	1.67	2.0	95.3	0.94
0.25	72.1	10.6	7.99	2.41	3.83	21.1	0.86
0.5	111.3	14.9	9.51	2.42	—	—	0.75
0.75	124.8	16.3	9.88	2.44	—	—	0.63
1.0	129.5	17.0	9.98	2.41	—	—	0.55
1.25	125.8	17.1	9.70	2.36	—	—	0.46
1.5	130.2	17.1	10.2	2.39	—	—	0.40
3.0	104.8	15.9	9.34	2.16	—	—	0.18
6.0	67.66	13.0	8.22	1.82	—	—	0.06
8.0	31.94	8.46	6.74	1.45	—	—	0.06
10.0	9.204	5.45	3.04	0.97	1.0	200	0.04

TABLE 6: Series C2: $\ell_B = 0.0\ldots6.0\sigma$, $f = 1/2$, $\epsilon = 1.75k_B T$, $N_m = 199$, $\rho_c = 5.0 \times 10^{-5}\sigma^{-3}$

ℓ_B	R_E	R_H	r	α	np	g_P	OC
0.0	4.41	3.27	2.22	0.91	1.0	199	0.97
0.167	4.63	3.30	2.39	0.91	1.0	199	0.93
0.333	14.2	4.59	3.72	1.60	1.87	102	0.82
0.5	26.6	5.72	5.38	2.00	2.90	61.4	0.79
1.0	54.7	8.90	7.53	2.24	4.80	25.0	0.57
1.5	65.2	10.4	8.22	2.19	—	—	0.45
2.0	66.4	10.8	8.40	2.12	—	—	0.36
2.5	62.6	10.5	8.52	2.04	—	—	0.27
3.0	59.9	10.3	8.48	2.00	—	—	0.21
3.5	54.2	9.84	8.26	1.92	—	—	0.16
4.0	48.0	9.23	8.08	1.83	—	—	0.13
6.0	27.8	6.96	7.03	1.50	—	—	0.06
9.0	7.45	4.37	3.16	0.96	1.14	173	0.05

TABLE 7: Series C3: $\ell_B = 0.0\ldots9.0\sigma$, $f = 1/3$, $\epsilon = 1.75k_B T$, $N_m = 199$, $\rho_c = 5.0 \times 10^{-5}\sigma^{-3}$

ℓ_B	R_E	R_H	r	α	np	g_P	OC
0.0	4.41	3.27	2.22	0.91	1.0	199	0.97
0.25	4.59	3.29	2.37	0.91	1.0	199	0.93
0.5	5.10	3.31	2.86	0.91	1.0	199	0.76
0.75	10.5	4.04	4.01	1.30	1.62	120	0.64
1.0	13.0	4.39	4.24	1.44	1.87	104	0.54
1.25	13.5	4.51	4.22	1.46	1.98	97.4	0.47
1.5	13.5	4.50	4.38	1.43	1.95	99.2	0.38
2.25	12.2	4.47	4.32	1.31	1.57	125	0.29
3.0	12.3	4.44	4.90	1.25	1.30	152	0.22
4.5	9.86	4.29	3.99	1.25	1.06	188	0.10
6.0	7.77	4.06	3.39	1.04	1.01	198	0.15
9.0	6.35	3.82	3.07	0.95	1.00	199	0.07

TABLE 8: Series C4: $\ell_B = 1.5\ldots12.0\sigma$, $f = 1/3$, $\epsilon = 1.5k_B T$, $N_m = 94$, $\rho_c = 1.0 \times 10^{-5}\sigma^{-3}$

ℓ_B	R_E	R_H	r	α	np	g_P	OC
1.5	13.5	3.93	5.33	1.49	2.04	41.2	0.68
1.8	13.9	4.00	5.47	1.48	2.10	39.6	0.62
2.1	15.1	4.15	5.88	1.50	2.24	36.2	0.59
2.4	15.7	4.23	6.14	1.50	2.27	35.3	0.49
2.7	15.6	4.22	6.41	1.46	2.26	35.9	0.53
3.0	15.6	4.23	6.47	1.45	2.26	35.8	0.40
3.3	14.4	4.10	6.43	1.39	2.17	38.5	0.45
3.6	13.2	3.97	6.22	1.33	2.06	41.6	0.30
3.9	12.2	3.85	6.17	1.28	1.92	45.6	0.33
5.1	8.6	3.44	5.08	1.10	1.38	66.7	0.22
5.4	8.2	3.39	5.06	1.08	1.30	71.2	0.17
5.7	8.0	3.37	4.96	1.07	1.26	73.6	0.08
6.0	7.7	3.34	4.81	1.05	1.22	76.4	0.12
9.0	5.7	3.14	3.58	0.97	1.03	91.4	0.19
12.0	5.1	3.06	3.17	0.94	1.01	93.4	0.04

TABLE 9: Series D: $\ell_B b^{-1} f^2 = 0.25 = \text{const.}$,
 $\epsilon = 1.75 k_B T$, $N_m = 200$, $\rho_c = 5.0 \times 10^{-4} \sigma^{-3}$

ℓ_B	f	R_E	R_H	r	α	np	g_P	OC
0.25	1.00	59.4	9.54	7.81	2.23	4.88	21.6	0.75
1.00	0.50	32.3	6.66	6.96	1.84	4.37	39.2	0.44
2.25	0.33	8.3	4.15	2.90	1.18	1.11	179	0.17
4.00	0.25	5.9	3.55	3.00	0.96	1.00	201	0.13